https://doi.org/10.5194/egusphere-2026-2324
Preprint. Discussion started: 15 June 2026

Joint Estimation of Creep and Slip for the Xiongba Landslide Based on InSAR Observations

Ying-Hui Yang[1], Qiang Xu[1], Qian Xu[2], Jyr-Ching Hu[3], Sha-Sha Tan[1], Qiang Chen[4], Lin Li[1]

1. State Key Laboratory of Geohazard Prevention and Geoenvironment Protection, Chengdu University of Technology, Chengdu, Sichuan, China
2. College of Air Traffic Management, Civil Aviation Flight University of China, Chengdu, Sichuan, China
3. Department of Geosciences, National Taiwan University, Taipei, Taiwan, R.O.C.
4. Department of Remote Sensing and Geoinformation Engineering, Southwest Jiaotong University, Chengdu, Sichuan, China

Correspondence to: Qian Xu (15902837201@163.com)

Abstract: Contact-based methods are employed used to monitor landslides, but their high cost, inefficiency, and reliance on discrete points limit a comprehensive understanding of landslide deformation behavior. To address this limitation, a geodetic inversion strategy integrating creep and dislocation models is proposed to estimate landslide creep and slip from InSAR observations, enabling the quantitative separation of their respective contributions to landslide motion. The method was applied to the Xiongba landslide in Gongjue County, Tibet. SBAS-InSAR-derived ascending and descending deformation of the Xiongba landslide was used to estimate creep and slip models via the proposed method. The results show that the Xiongba landslide is dominated by slope-aspect motion, with a maximum rate of 495 mm/yr, and secondary landslide bodies H1 and H2 exhibit distinct movements but share similar viscosity parameters. The inversion results indicate that surface deformation of the Xiongba landslide is predominantly controlled by slip processes, whereas the contribution of mass creep is comparatively limited. Model misfits of 7.9 (ascending) and 4.7 (descending) mm/yr indicate good agreement with observations, and the alignment between estimated and observed slip depths further supports the model's reliability. The proposed inversion framework provides a new means of disentangling creep and slip contributions to landslide deformation and offers valuable insights into the failure mechanisms governing large-scale landslides.

Keywords: Xiongba Landslide; Time-series InSAR Deformation; Joint inversion method; Creep model; Slip model

1 Introduction

Landslides are severe geological hazards involving the downward movement of materials, controlled by a combination of geological formations, climate changes, and human activities (Song et al., 2022). Owing to their sudden onset, concealed development, and potentially widespread impacts, landslides pose significant threats to human life and property (Crozier, 2010). Landslide activity has increased in recent years, due to rapid urbanization, intensified engineering activities, glacier melting, and more frequent extreme rainfall events (Lin et al., 2022). Consequently, landslides have become one of the major challenges threatening infrastructure development and engineering activities, particularly in road construction, water conservancy projects, and mining (Crozier, 2010, Zhu et al., 2024). Understanding landslide movement processes and deformation

https://doi.org/10.5194/egusphere-2026-2324
Preprint. Discussion started: 15 June 2026

mechanisms is therefore essential for hazard assessment, early warning, and risk mitigation.

Techniques for detecting and monitoring internal landslide movement can generally be categorized into contact and non-contact methods. Contact methods, such as slope inclinometers and Time Domain Reflectometry (TDR), have been widely used for monitoring internal landslide movement (Su, 1987; Drahor et al., 2006; Simeoni & Mongiovì, 2007; Stark & Choi, 2008;). However, these methods are generally costly, labor-intensive, and time-consuming. Moreover, they provide deformation measurements only at discrete locations, making it difficult to characterize the overall movement behavior of an entire landslide. Their applicability is also limited for steep, inaccessible, or hazardous landslides where field investigations are challenging.

Compared with contact-based approaches, non-contact methods are generally more efficient and less labor-intensive. Representative non-contact methods include the equilibrium cross-section method (Bishop, 1999), the dislocation method (Nikolaeva et al., 2014), the non-Newtonian viscous flow method, limit equilibrium method and the mass conservation method (Zhu et al., 2024). These methods characterize landslide behaviors by integrating surface displacement observations and soil parameters within modeling frameworks. Recent studies have made significant progress in landslide movement modeling and parameter estimation (Aryal et al., 2015; Hu et al., 2018; Zhu et al., 2024). It has been clarified that landslide deformation is driven by the combined effects of internal creep and slip processes. However, most existing approaches consider only one of these processes, neglecting their coupled contribution.

The Xiongba Ancient Landslide is located on the right bank of the Jinsha River in Gongjue County, Tibet, within a steep V-shaped valley with elevations of approximately 2600–4000 m and local slopes exceeding 60°. The area is highly susceptible to landslides due to its complex geological and climatic conditions. The Xiongba Landslide covers an area of about 5.33 km² and is situated near major transportation corridors, posing potential risks to regional infrastructure and downstream communities. Previous borehole surveys and soil strength tests revealed high moisture content and low plastic limits within the landslide materials, indicating that the slip surface has long remained in a semi-solid state and is prone to creep deformation (Jin, 2021). InSAR observations further showed notable deformation and damage, particularly in the middle and frontal parts of the landslide, suggesting that it is generally in an unstable state and may pose a risk of large-scale sliding failure and river blockage under extreme weather conditions (Wu et al., 2024).

In this study, a joint inversion method is proposed to characterize both the creep and slip behaviours of the Xiongba landslide based on the InSAR-derived ground deformation rates. The InSAR deformation fields are derived from ascending and descending Sentinel-1 InSAR data, using the SBAS-InSAR technique. Both the Bingham creep and elastic dislocation models are incorporated in this method, enabling the mathematical modeling of the relationship between complex landslide movement and surface deformation. The reliability of our inversion results is validated through misfit analysis and by comparing the estimated slip depth with borehole measurements. The inversion results characterize both the depth-dependent creep behavior and sliding surface slip distribution, offering scientifically-grounded support for Xiongba landslide risk management strategies.

https://doi.org/10.5194/egusphere-2026-2324
Preprint. Discussion started: 15 June 2026

2 Overview and Data Processing Workflow of the Xiongba Landslide

2.1 Study Area

The Xiongba landslide is located in Shadong Township, Gongjue County, Tibet Autonomous Region, China. The Jinsha River flows from north to south along the front edge of the landslide (Fig. 1a). The topography is characterized by plateau mountains, hills, and deep canyons, shaped by the intense incision of the Jinsha River. The terrain is steep, with poorly developed terraces, and is classified as an extremely high mountain landscape. The is characterized by a continental plateau monsoon climate zone, with an average annual temperature of approximately 6.5°C and an average annual precipitation of about 480 mm, most of which occurs between May and September. Studies suggest that intense rainfall may induce landslide movement along internal weak layers, posing risks such as river blockage or dam-break events, which endanger nearby settlements (Li et al., 2021; Lv et al., 2025; Yan et al., 2024).

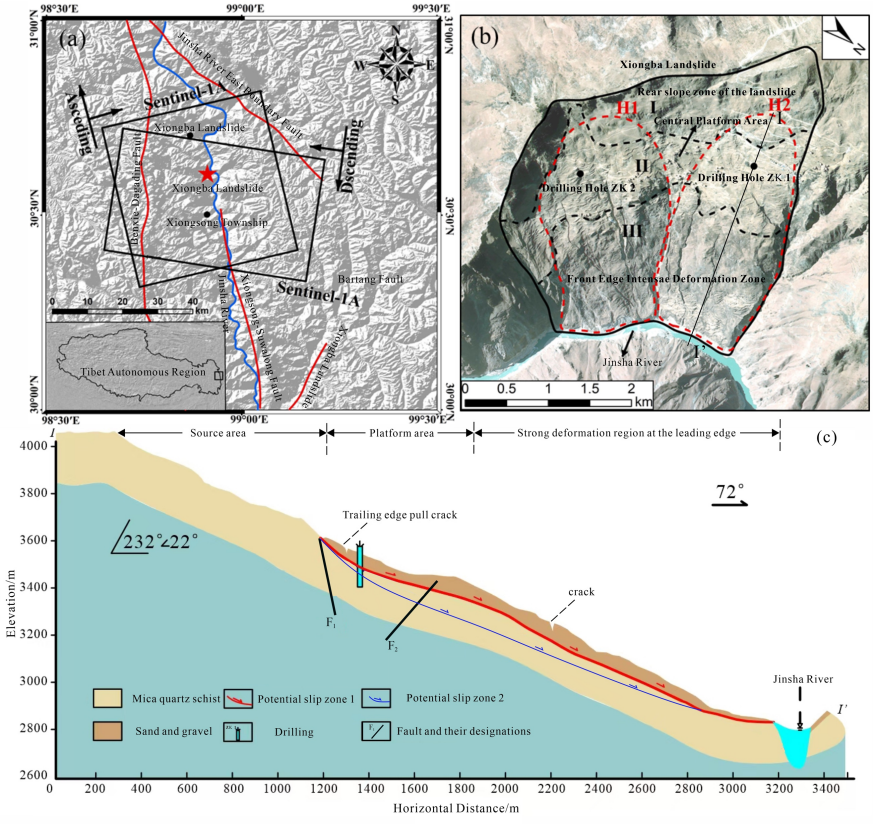

Figure 1. Study area of the Xiongba ancient landslide. (**a**) SAR image coverage, (**b**) optical image, and (**c**) geological profile from the study by Jin (2021).

The Xiongba landslide displays a circular, chair-shaped geometry. The front edge is bounded by the Jinsha River, which has subjected the slope to significant fluvial erosion, while the rear edge is defined by a mountain ridge, resulting in a vertical elevation difference of approximately 1150 m. The landside has an overall length of approximately 2500 m and an average width of about 2800 m,

https://doi.org/10.5194/egusphere-2026-2324
Preprint. Discussion started: 15 June 2026

covering an area of roughly 6.72 km². The average slope gradient ranges from 15° to 30°. Based on topographic features, the landslide is divided into a source area, a platform area, and a front-edge deformation zone (Fig. 1c). The source area is relatively stable, with exposed bedrock; the platform area has a gentler slope and serves as the main residential zone; the front-edge area has steeper slopes, prominent tension cracks, erosion gullies, and local collapses.

The Xiongba landslide lies within the Jinsha River seismic zone, which hosts several active faults (Guo et al., 2021; Yang et al., 2024). The Jinsha River fault zone, together with the Luona–Buxu fault, passes through the central and rear portions of the Xiongba landslide. The landslide predominantly exposes strata composed of mica–quartz schists from the Lower Permian Gangtuoyan Formation (PT_{1g}), with residual Quaternary sand and gravel present at the surface. The riverbed sediment of the Jinsha River primarily consists of Quaternary alluvial–proluvial deposits (Q_4^{al+pl}). Due to the historical activity of the Jinsha River fault zone, the rock masses in this area are extensively fractured, resulting in highly variable stratum occurrences. In addition, continuous fluvial erosion at the landslide toe further promotes slope instability (Yan et al., 2021; Zheng et al., 2024).

2.2 SAR Data and Processing

In this study, a series of SAR images in interferometric wide-swath (IW) mode captured by the Sentinel-1 satellite were utilised to map the surface deformation fields of the Xiongba landslide, including 59 ascending-track and 68 descending-track. The coverage of the used SAR data is shown in Fig. 1a, and detailed parameters are listed in Table 1. To ensure high-precision deformation measurements, the Precise Orbit Ephemerides (POD) data were used to refine satellite orbit vectors. The high-resolution digital elevation model (DEM) with a 30 m resolution provided by the Japan Aerospace Exploration Agency (JAXA) was employed to simulate and remove the topographic phase component. Phase unwrapping was performed using the minimum cost flow algorithm (Costantini & Rosen, 1999; Pepe et al., 2011). Furthermore, tropospheric delay data with a spatial resolution of 90 m, from the Generic Atmosphere Correction Online Service for InSAR (GACOS) system, were used to mitigate atmospheric phase delays.

Table 1. Parameters of the Sentinel-1A SAR images used in this study.

Flight direction	Scenes	Incidence angle (˚)	Heading (˚)	Time span
Ascending	59	33.85	349.5	20200102-20220316
Descending	68	39.28	190	20200321-20220323

https://doi.org/10.5194/egusphere-2026-2324
Preprint. Discussion started: 15 June 2026

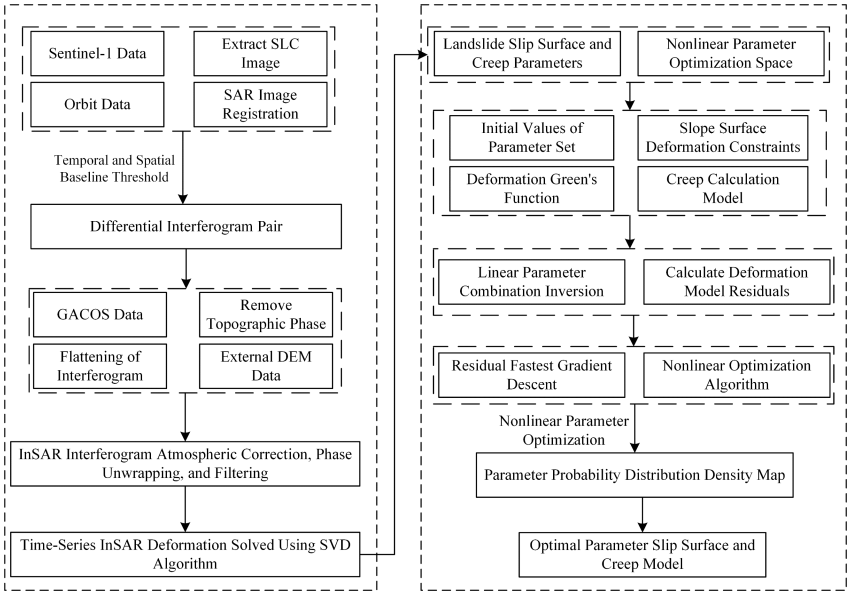

Figure 2. Flowchart of the InSAR time-serie data processing and joint inversion procedure for creep and slip models.

A total of 445 ascending-track and 587 descending-track interferometric pairs were generated for time-series analysis, with temporal baselines of up to 120 days and spatial baselines within 300 m. The small baseline subset (SBAS) InSAR time-series technique enabled the extraction of ground deformation in the Xiongba landslide area (Berardino et al., 2002), implemented through the Miami INsar time-series software in Python (MintPy; Yunjun et al., 2019). The MintPy processing workflow incorporates both high-pass and low-pass filtering strategies to reduce atmospheric delays. Topographic residuals were mitigated by exploiting their correlation with the perpendicular baseline time series, simultaneously partially correcting for orbital phase errors (Fattahi & Amelung, 2013; Yunjun et al., 2019). The detailed steps of the SAR data processing are shown in the left panel of Fig. 2. Finally, the derived ground deformation and velocity fields can be found in Figs. 4 and 5.

3 Methods

3.1 Components of Surface Deformation on A Landslide

The observed surface deformation on a landslide consists of two main components governed by distinct mechanical mechanisms. One component, denoted as u_r, is the gravitational deformation caused by mass rock creep, which can be quantitatively described using a creep model (Angeli et al., 1996; Han et al., 2014). The other component, designated as u_s, represents deformation controlled by slip along the sliding surface and can be modeled based on the dislocation theory (Okada, 1985). The total ground deformation u can be described as the sum of u_r and u_s, as expressed in Eq. (1). A schematic diagram illustrating the two different components of deformation on a landslide surface, caused by different mechanisms, is shown in Fig. 3a.

$$u = u_r + u_s \tag{1}$$

The dislocation theory proposed by Okada (1985) is applied to calculate the slip-induced

https://doi.org/10.5194/egusphere-2026-2324
Preprint. Discussion started: 15 June 2026

surface deformation component. This component is influenced by the spatial location and geometric parameters of the sliding surface (Okada, 1985; Muller et al., 2000; Nikolaeva et al., 2014; Aryal et al., 2015). The Bingham model is used to calculate the creep deformation component of the slope body (Han et al., 2014; Li et al., 2022; Balmforth et al., 2014; Huang et al., 1998), as illustrated in Eq. (2). In Eq. (2), J denotes the Bessel function, μ_m is the m-th zero value of the Bessel equation $J_{-b}(x)=0$, η_0 is the viscosity parameter of the soil under saturated conditions, b is a parameter that describes the depth-dependent nonlinear behavior in viscosity, ρ inidactes the soil density, t represents time, and H denotes the depth of landslide creep.

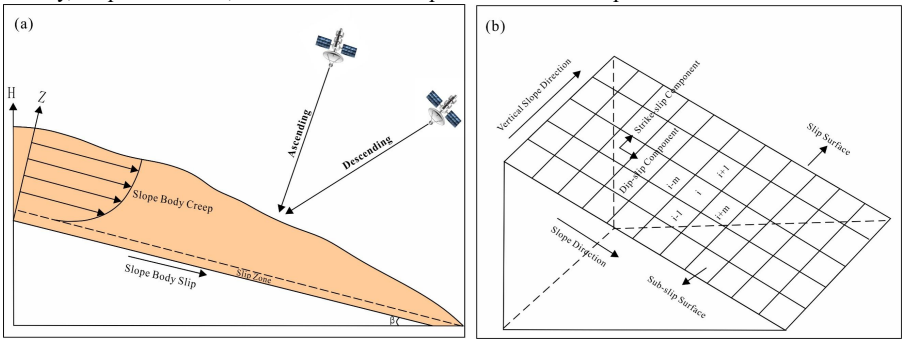

Figure 3. (**a**) Schematic of Landslide Surface Deformation Components govern by different mechanisms. (**b**) Sliding surface finite element model.

$$v(z,t)=\frac{32AH^{\frac{3-b}{2}}}{\eta_0}\times\sum_{m=1}^{\infty}\left\{B_m z^{\frac{1-b}{2}}J_{1-b}(\mu_m\sqrt{z/H})[1-\exp(-\frac{\eta_0\mu_m^2}{4\rho H}t)]\right\} \tag{2}$$

3.2 Joint Inversion for Landslide Creep and Slip models

Two-step strategy is applied to conduct the geodetic inversion for landslide creep and slip models. The first step involves performing nonlinear optimization of the model parameters, including the geometric parameters of the slip surface (e.g. dip angle, depth) and the geomechanical properties of the landslide body (e.g. cohesion, internal friction angle, viscosity). Due to the strong nonlinearity between these parameters and measured InSAR ground deformation, global optimization algorithms such as simulated annealing and genetic algorithms are applied. The second step is the inversion for the detailed slip distribution. After the best-fitting model parameters are obtained, a finite element model of the slip surface is established, from which the Green's function relating slip movement to surface deformation can be computed. Then, the slip distribution along the sliding surface can be derived using a least-squares approach (Yang et al., 2018). The detailed procedures are as follows:

In the optimization of model parameters, the deformation response Green's function G_{ij} and the creep u_{rj} are computed using Eq. (3). In Eq. (3), K_i represents the geometric size and location of the slip surface, N denotes the mechanical properties of the slip surface, α and β are respectively the strike angle and dip angle of the slip surface, f_r is the surface deformation expression resulting from a rectangular dislocation source, η_0 and b are viscosity-related parameters; and I_j represents the depth of the slip surface beneath a surface point j.

$$\begin{cases} G_{ij}=f_S(K_i,\beta,I_j) \\ u_{rj}=f_r(\eta_0,b,I_j,\beta,N) \end{cases} \tag{3}$$

https://doi.org/10.5194/egusphere-2026-2324
Preprint. Discussion started: 15 June 2026

After the optimal parameters are determined by the nonlinear optimization, the geometry of the slip surface is fixed. Then, the slip surface can be discretized using a small spatial size (Fig. 3b). Let A denotes the covariance matrix of u_s. The least-squares solution for the slip vector is given by Eq. (4) (Sabharwal et al., 1998; Xu et al., 2011; Ji et al., 2021).

$$\hat{s} = \left[G^T A^{-1} G\right]^{-1} G^T A^{-1} u_s \tag{4}$$

To prevent sharp gradients in the slip magnitude between adjacent slip sub-patches, a Laplacian smoothing constraint is introduced into the inversion model (Jonsson, 2002; Funning et al., 2005; Min et al., 2014; Chen et al., 2011). The detailed formulation of our geodetic inversion is provided in Eq. (5), where L_1 and L_2 are the Laplacian smoothing matrices for the strike-slip and dip-slip components, respectively, G_1 and G_2 are the Green's function matrices for the strike-slip and dip-slip components, and S_1 and S_2 represent the strike-slip and dip-slip vectors. In addition, the detailed inversion procedure is shown in Fig. 2.

$$\begin{bmatrix} u_s \\ 0 \\ 0 \end{bmatrix} = \begin{bmatrix} G_1 & G_2 \\ L_1 & 0 \\ 0 & L_2 \end{bmatrix} \begin{bmatrix} s_1 \\ s_2 \end{bmatrix} \tag{5}$$

4 Result and Discussion

4.1 Ascending and Descending InSAR Velocity Fields of the Xiongba Landslide

Figure 4 presents the InSAR-derived ground deformation rate fields of the Xiongba landslide SBAS-InSAR analysis. Figures 4a and 4b display the ascending and descending line-of-sight (LOS) velocity fields, respectively. In both figures, positive values represent a decrease in slant range, indicating surface movement toward the satellite, while negative values represent an increase, indicating movement away from the satellite. Notable differences in both the magnitude and spatial distribution of deformation were observed between the two InSAR tracks. The deformation rates derived from the ascending track range from -212 mm/yr to 13 mm/yr, yielding a maximum variation of 225 mm/yr. In comparison, the descending track shows a range from -117 mm/yr to 79 mm/yr, with a maximum difference of 196 mm/yr. These differences arise from the distinct side-looking imaging geometries of the ascending and descending tracks. The Xiongba landslide area, with its significant topographic variations, further influences the SAR imaging geometry. The differing viewing angles of the two tracks lead to varying degrees of distortion, such as shadowing and layover, which in turn affect the deformation fields.

In Addition, both positive and negative values can be found in the descending velocity field, indicating differing deformation directions between the northern and southern portions of the slopes. These differences can be attributed to variations in slope and aspect angles between the two flanks of the Xiongba landslide, with negative values observed on the southern slope and positive values on the northern slope in the descending InSAR track. Optical imagery interpretation (Fig. 1b) further divides the Xiongba landslide into two secondary bodies, H1 and H2, separated by erosion gullies and distinct aspect angles. This division is corroborated by the descending InSAR observations, which reveal contrasting deformation patterns on either side, suggesting kinematic independence between the two units.

https://doi.org/10.5194/egusphere-2026-2324
Preprint. Discussion started: 15 June 2026

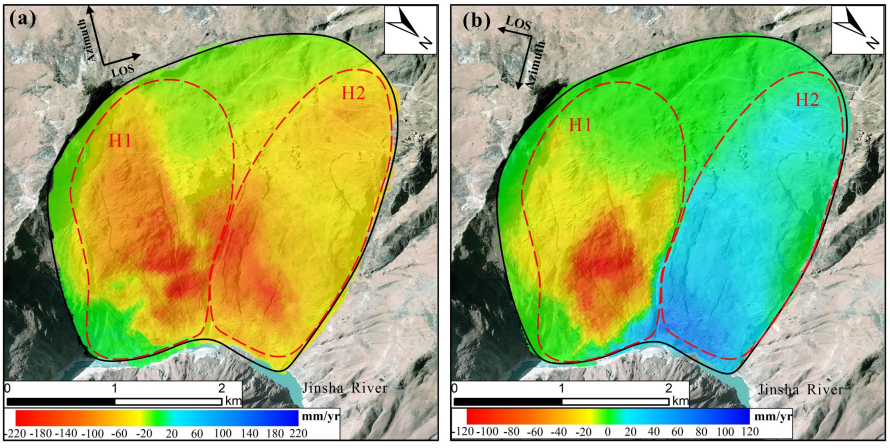

Figure 4. Ascending (**a**) and descending (**b**) InSAR deformation rate fields of the Xiongba landslide.

4.2 Analysis of Deformation Characteristics of the Xiongba Landslide

Figure 5 presents the time series deformation from ascending and descending InSAR tracks, with cumulative deformation recorded at four-month interval. The results reveal significant differences in both the magnitude and spatial distribution of the accumulated deformation between the two tracks. The ascending data indicate the ground movements away from the satellite, whereas the descending measurements reveal that both the northern and southern slope bodies are moving downslope consistent with their respective aspect angles. Due to its viewing geometry, the ascending track is more sensitive to landslide movement, as evidenced by a wider range of cumulative deformation (-465 mm to 30 mm), compared to the descending track, which shows a narrower range (-250 mm to 167 mm).

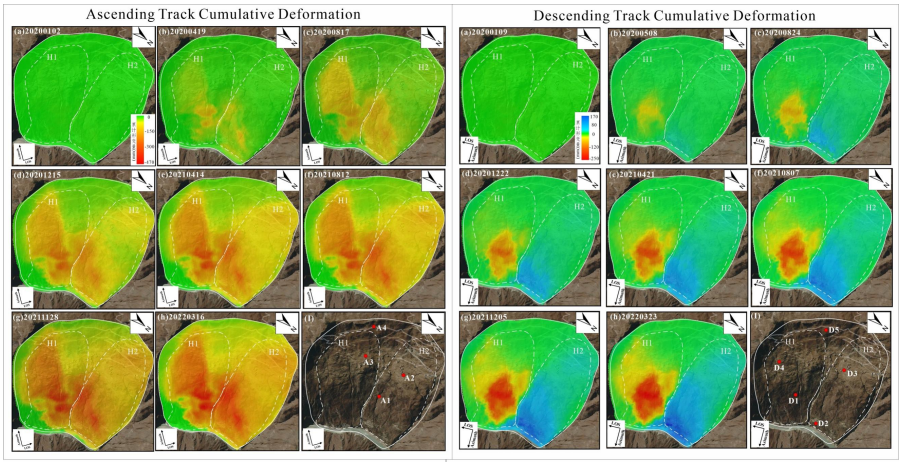

Figure 5. Time series LOS deformation fields from the Sentinel-1 ascending and descending InSAR tracks.

https://doi.org/10.5194/egusphere-2026-2324
Preprint. Discussion started: 15 June 2026

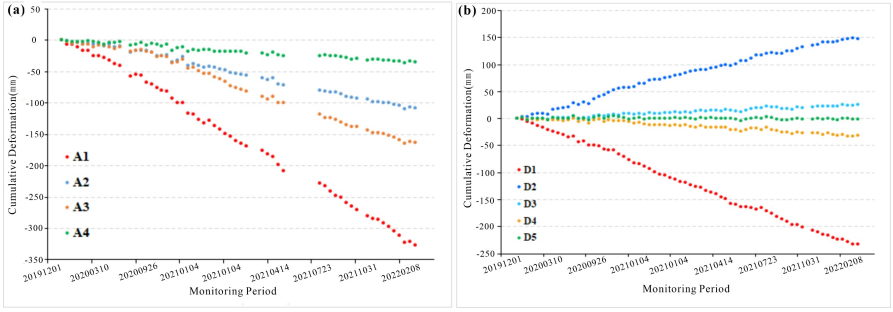

Figure 6. Displacement time series of target points A1-A4 (marked in Fig. 5) from the ascending (**a**) InSAR, and D1-D5 (marked in Fig. 5) from the descending (**b**) InSAR.

Both ascending and descending InSAR observations effectively capture the characteristics of ground deformation associated with the Xiongba landslide. Based on the observed deformation features, the landslide can be subdivided into three distinct zones: (1) a front steep-slope zone exhibiting pronounced deformation, (2) a middle platform zone with moderate deformation, and (3) a relatively stable rear zone, as shown in Fig. 7a. In the front zone, where the slope is steep, vegetation is sparse, and the continuous erosional impact of the Jinsha River reduces slope stability, the time-series displacements of points A1, D1, and D2 (Fig. 6) exhibit linear deformation trends with substantial magnitudes. In contrast, the middle platform experiences relatively lower deformation, as indicated by the time-series displacements of points A2, A3, D3, and D4, primarily influenced by the instability in the front zone. In the rear zone, the time-series displacements of points A4 and D5 are minimal, illustrating the relative stability of this region.

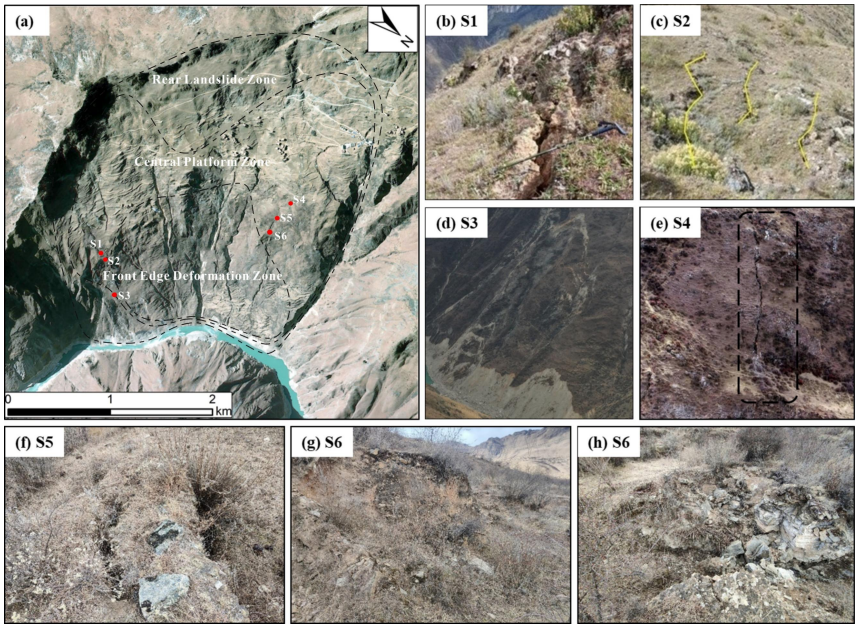

Figure 7. Field deformation characteristics of the Xiongba landslide. (**a**) Distribution of field deformation features; (**b**)-(**h**) Field photographs of deformation features.

https://doi.org/10.5194/egusphere-2026-2324
Preprint. Discussion started: 15 June 2026

Field investigation (Fig. 7) reveals that multiple transverse cracks—some up to 15 cm wide—have developed on the southern slope. At the toe of the slope, localized collapse and sliding bodies exhibit a multi-phase failure pattern, as shown in Figs. 7b-d. On the northern slope, longitudinal cracks extend for ~150 m, while a transverse tension crack—measuring 10–50 cm in width and up to 350 m in length—has developed near the slope center, accompanied by a prominent back scarp (Figs. 7e-h). These field observations are consistent with the spatial deformation patterns revealed by InSAR, thereby confirming the reliability of the InSAR measurements and underscoring the role of aspect angle in controlling deformation behavior.

In summary, the Xiongba landslide is currently experiencing slow but progressive deformation, with the most pronounced motion concentrated at the slope's front edge. Should destabilization occur in this region, it could potentially trigger secondary hazards such as river damming or collapse, posing serious threats to nearby communities. Therefore, particular attention should be paid to the deformation evolution of the frontal zone. Moreover, the impacts of rainfall, groundwater movement, and geological structure must be comprehensively considered to enhance landslide monitoring and early warning systems, thereby providing a scientific basis for disaster prevention and risk mitigation.

4.3 Creep and Slip Estimation of the Xiongba Landslide

The geodetic inversion is performed using the proposed method in section 3. The model parameters for the landslide bodies H1 and H2 are required to be determined first. To enable comparison and validation against existing survey data, the reference points for the H1 and H2 models were selected at the locations of boreholes ZK1 and ZK2 from the study by Jin (2021). Parameter optimization was carried out using the simulated annealing algorithm, with the parameter search ranges defined in Table 2. The final optimized parameters for landslide bodies H1 and H2 are listed in Table 3.

Table 2: Search space for optimal parameter estiamtion of H1 and H2.

Parameter	Xiongba-H1	Xiongba-H2
Dip angle (°)	[22, 27]	[22, 27]
Slip surface depth (m)	[-80, -20]	[-80, -20]
Rake angle (°)	[-140, -50]	[-140, -50]
Viscosity parameter η_0 ($\times 10^9$)	[0, 20]	[0, 20]
Viscosity parameter b	[0, 1]	[0, 1]

Table 3. Optimal parameters for H1 and H2 derived from InSAR measurements.

Parameter	Xiongba-H1		Xiongba-H2	
	Optimal parameter value	Parameter uncertainty	Optimal parameter value	Parameter uncertainty
Dip angle (°)	24.2	0.08	23.8	0.09
Slip Surface Depth (m)	-53.2	1.39	-46.3	1.44
Rake angle (°)	-75.1	1.56	-102.8	2.10
Viscosity parameter η_0 ($\times 10^9$)	14.1	0.42	13.1	0.40
Viscosity parameter b	0.72	0.02	0.69	0.02

https://doi.org/10.5194/egusphere-2026-2324
Preprint. Discussion started: 15 June 2026

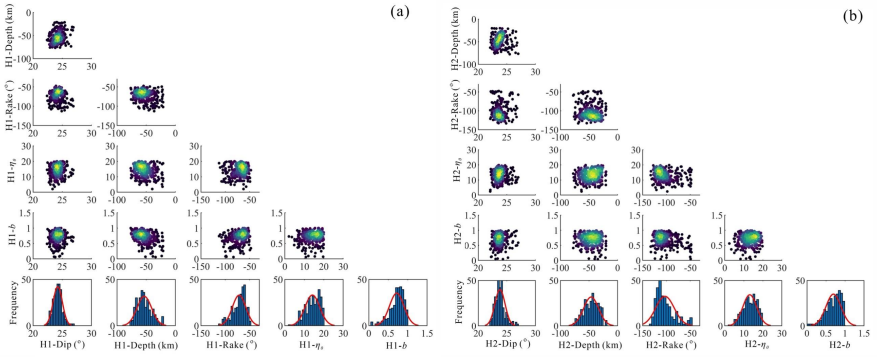

Figure 8. Posterior probability distributions of optimized parameters: H1 (**a**) and H2 (**b**).

Through iterative searches, parameter groups that minimized model residuals were obtained. To mitigate the risk of convergence to local optima, the simulated annealing algorithm was repeatedly executed with varied initial parameter sets. The probability density distribution was subsequently generated based on these parameter groups, and the set corresponding to the maximum likelihood was identified as the optimal model solution. As shown in Fig. 8, the joint distributions of the parameters exhibit clear clustering, indicating that the parameter search process has converged. The parameters display a high degree of independence, and the multiple solutions closely follow a normal distribution, validating the reliability of the estimated parameters.

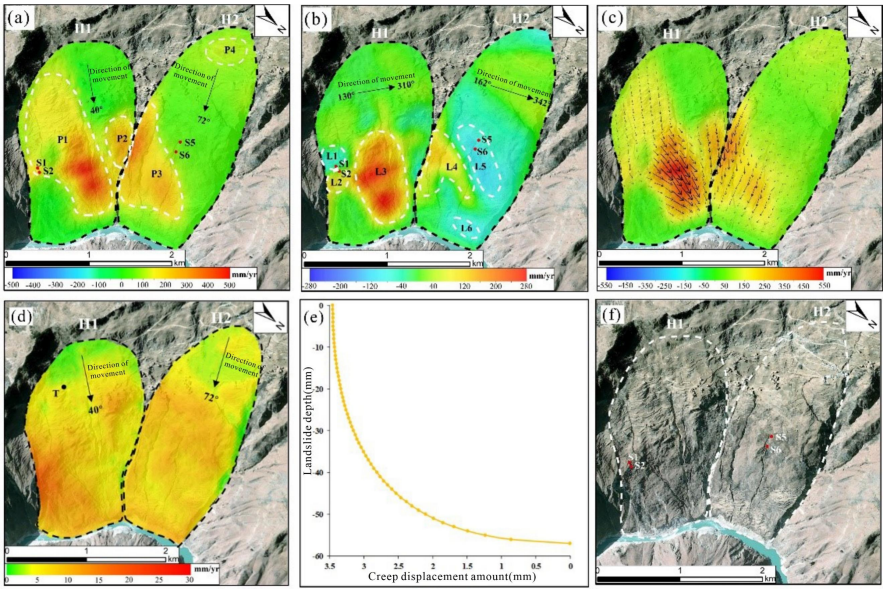

Figure 9. Slip and creep characteristics of the Xiongba landslide. (**a**) Dip-slip distribution map, (**b**) Strike-slip distribution map, (**c**) Total-slip distribution map, (**d**) Forward calculation of surface deformation rates induced by creep, (**e**) Creep-induced deformation with depth at Point T, marked in (d), (**f**) Optical image.

The estimated slip surface depths for the H1 and H2 landslides were 58.5 m and 50.9 m, respectively, closely matching the field borehole observations (55.5 m for H1 and 51.5 m for H2),

https://doi.org/10.5194/egusphere-2026-2324
Preprint. Discussion started: 15 June 2026

further demonstrating the high accuracy of the parameter estimation. Moreover, the viscosity parameters of the landslide bodies H1 and H2 are found to be highly similar, suggesting comparable material composition and mechanical properties. Given the spatial proximity of two slopes and their exposure to similar internal and external conditions, the consistency of these parameters is reasonable and expected.

Figures 9(a-c) exhibit the slip characteristics along the slip surfaces of Xiongba landslide bodies H1 and H2. The dip-slip distribution map (Fig. 9a) reveals the displacement pattern along the landslide aspect directions (40° for H1, and 72° for H2), while the strike-slip distribution (Fig. 9b) reflects lateral movement perpendicular to the aspect directions. Figure 9c presents the total-slip distributions, clearly indicating that the Xiongba landslide is primarily controlled by dip-slip movement along the slope. For slope H1, the dip-slip rates range from 80 mm/yr to 495 mm/yr, with the most active regions concentrated in areas P1 and P2. The strike-slip component for H1 is mainly located in three regions L1–L3, with rates ranging from -76 mm/yr to 278 mm/yr. For slope H2, dip-slip movement is primarily concentrated in region P3, adjacent to H1, with slip rates varying from 80 mm/yr to 367 mm/yr. The strike-slip component for H2 is comparatively smaller, with limited activity (less than 100 mm/yr) observed in regions L4 to L6. Positive rates are observed in L4, while negative rates characterize L5 and L6. These differences in slip magnitude and spatial distribution highlight distinct movement behaviors between the two landslide bodies.

Figure 9c illustrates the total-slip vector distribution along the Xiongba landslide, with black arrows indicating the direction and magnitude of the slip motion. This slip is primarily concentrated in the central to frontal portions of the slope. Comparsions between the modeled slip distributions and field-observed deformation features reveal that the surface cracks S1 and S2 (on slope H1, Fig. 9f) are located at the junction between regions L2 and L3, which exhibit opposite slip directions. Moreover, the crack S5 and steep scarp S6 on the slope H2 (Fig. 9f) are situated near the boundary of the high-slip region P3. These alignments indicate that the surface deformation features exhibit a certain spatial correspondence with the estimated slip distribution.

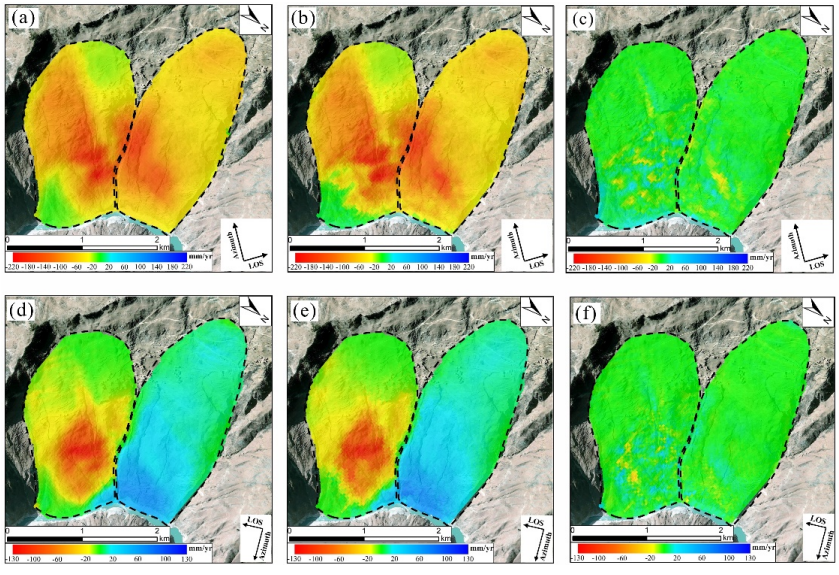

Figure 10. Forward modeling of surface deformation for the Xiongba landslide. Forward calculations of slip-induced

https://doi.org/10.5194/egusphere-2026-2324
Preprint. Discussion started: 15 June 2026

deformation from ascending (**a**) and descending (**d**) InSAR tracks. Observed ascending (**b**) and descending (**e**) InSAR deformation. (**c**) and (**f**) are the related residuals between the modeled and observed deformation rates.

To further quantitatively assess the reliability of the inversion results, forward modeling was performed using the estimated model to simulate the landslide surface deformation, which was then compared with observations to evaluate model residuals. Based on the Bingham model and estimated geotechnical parameters, the creep-induced surface deformation rates are calculated and presented in Fig. 9d, with an average rate of approximately 18 mm/yr. Figures 10(a) and 10(d) display the ground velocities predicted from the slip model. It is evident that the deformation induced by slip is significantly greater than that caused by creep, indicating that the surface deformation of the Xiongba landslide is primarily controlled by slip along the sliding surface. Moreover, Fig. 9e shows that the creep-induced ground deformation varies with depth, exhibiting a power-law distribution.

The comparison between the modeled (Figs. 10a, 10d) and observed (Figs. 10b, 10f) InSAR deformation fields reveals a high consistency in both spatial distribution and deformation magnitude. However, differences can be identified in the central to frontal portion of the landslide, particularly at the frontal region of H1, where the deformation induced by the creep model is most pronounced. The residual distributions, derived by subtracting the observed ground deformation from the deformation simulated under the combined effects of slip and creep, are presented in Figs. 10c and 10f. The residuals for the ascending (Fig. 10c) and descending (Fig. 10f) InSAR tracks are approximately 7.9 mm/yr and 4.2 mm/yr, respectively, indicating that the derived creep and slip model effectively explains the observed deformation, thereby supporting the reliability of the joint inversion in this study.

Although the modeled InSAR deformation aligns well with the observed data, some residual discrepancies remain. These can be attributed to several factors: (1) Simplification of slip surface geometry—the actual slip surface is likely to be irregular, while the model assumes a planar geometry, potentially introducing systematic errors; (2) Limitations of the deformation model—the dislocation and Bingham creep models used in this study cannot fully capture plastic deformation or potential accelerated creep, thereby affecting the accuracy of the inversion; (3) Uncertainty in InSAR observations—issues such as coherence loss, atmospheric delay, and phase unwrapping errors may introduce biases into the time series deformation extraction, contributing to the residuals.

5 Conclusion

In this study, a joint inversion of the creep and slip models of the Xiongba landslide is conducted, constrained by the surface InSAR observations. The ascending and descending LOS deformation fields are extracted using the SBAS-InSAR technique. The maximum absolute deformation rates for the ascending and descending InSAR tracks are 212 mm/yr and 117 mm/yr, respectively. Three distinct zones are identified within the landslide body: a frontal zone exhibiting the most significant deformation, a middle zone with moderate deformation, and a rear zone that remains relatively stable. The results indicate that the Xiongba landslide is currently undergoing slow deformation, following an approximately linear trend within the monitoring period.

A joint inversion framework integrating the Bingham creep model and elastic dislocation theory is proposed. The model misfits for the ascending and descending InSAR are 7.9 mm/yr and 4.7 mm/yr, respectively, indicating the validity of the proposed method. Moreover, the estimated

https://doi.org/10.5194/egusphere-2026-2324
Preprint. Discussion started: 15 June 2026

slip surface depths align closely with the field borehole data, futher verifying the accuracy of the derived model. The results show that slip motion primarily occurs along the landslide aspect direction, with a maximum rate of 495 mm/yr observed on the secondary landslide body H1. Although the two secondary bodies (H1 and H2) present distinct movement behaviors, their viscosity parameters remain highly similar. The creep-induced ground deformation exhibits a power-law distribution with depth. Furthermore, our findings validate that the surface movement of the Xiongba landslide is primarily controlled by slip along the sliding surface rather than mass creep, deepening the understanding of the landslide's kinematic mechanism.

Financial support. This research is supported by the National Natural Science Foundation of China (Grant No. 42474041 and 42471485), Sichuan Province Philosophy and Social Science Planning Major Project, China (SCJJ23WT06), State Key Laboratory of Geohazard Prevention and Geoenvironment Protection Independent Research Project (SKLGP2021Z016), Science and Technology Plan Projects of Tibet Autonomous Region (XZ202403ZY0014).

Author Contributions. Conceptualization: Ying-Hui Yang, Qiang Xu; methodology, Ying-Hui Yang, Qian Xu; investigation, Qian Xu, Sha-Sha Tan, Lin Li; data curation, Qian Xu, Lin Li; writing original draft preparation, Qian Xu; writing–review and editing, Ying-Hui Yang, Qiang Xu, Jyr-Ching Hu, Qiang Chen; visualisation, Sha-Sha Tan; supervision, Ying-Hui Yang; funding acquisition, Ying-Hui Yang.

Data availability. The Sentinel-1 SAR images are available at https://search.asf.alaska.edu/#/, accessed on 27 April, 2025. The DEM data used in the InSAR data processing are available at https://www.eorc.jaxa.jp/ALOS/en/dataset/aw3d_e.htm, accessed on 29 September, 2025, registration is required for free access. The GACOS data is freely available here: https://www.gacos.net, accessed on 20 September, 2025.

Competing interests. The authors declare no competing interests.

Acknowledgments. All the figures are mapped based on the Generic Mapping Tools (GMT) software (Wessel and Smith, 1998). The authors used ChatGPT (OpenAI) solely for language editing and polishing. The authors take full responsibility for the content of the manuscript.

References

Angeli, M. G., Gasparetto, P., Menotti, R. M., Pasuto, A., & Silvano, S. (1996). A visco-plastic model for slope analysis applied to a mudslide in Cortina d'Ampezzo, Italy. *Quarterly Journal of Engineering Geology and Hydrogeology*, 29(3), 233-240.

Aryal A., Brooks B. A., Reid M. E. (2015). Landslide subsurface slip geometry inferred from 3-D surface displacement fields [J]. *Geophysical Research Letters*, 42(5): 1411-1417.

Bai D. X., Lu G. Y., Hu H. H., Lin H., Chen C. F., Wang X. (2024). Deformation Analysis and Reinforcement Effect Evaluation for the No. 65 Slope on the Shangsan Expressway Based on SBAS-InSAR. *Buildings*, 14(11):3582.

Balmforth N. J., Frigaard I. A., Ovarlez G. (2014). Yielding to Stress: Recent Developments in Viscoplastic Fluid Mechanics. *Annual Review Of Fluid Mechanics*, 46(1):121-146.

https://doi.org/10.5194/egusphere-2026-2324
Preprint. Discussion started: 15 June 2026

Berardino, P., Fornaro, G., Lanari, R., & Sansosti, E. (2002). A new algorithm for surface deformation monitoring based on small baseline differential SAR interferograms. *IEEE Transactions on geoscience and remote sensing*, 40(11), 2375-2383.

Bishop, K.M. (1999). Determination of translational landslide slip surface depth using balanced cross sections. *Environ. Eng. Geosci*, 2, 147–156.

Chatterjee R. S., Thapa S., Singh K. B.,Varunakumar G., Raju E. V. R. (2015). Detecting, mapping and monitoring of land subsidence in Jharia Coalfield, Jharkhand, India by spaceborne differential interferometric SAR, GPS and precision levelling techniques. *J Earth Syst Sci,* 124:1359–1376.

Chen Y., Nasrabadi N. M., Tran T. D. (2011). Hyperspectral Image Classification Using Dictionary-Based Sparse Representation. *IEEE Transactions on Geoscience and Remote Sensing*, 49(10):3973-3985

Costantini, M., & Rosen, P. A. (1999). A generalized phase unwrapping approach for sparse data. In *IEEE 1999 International Geoscience and Remote Sensing Symposium. IGARSS'99 (Cat. No. 99CH36293)* (Vol. 1, pp. 267-269). IEEE.

Crosetto M., Solari L., Mroz M., Balasis-Levinsen J., Casagli N., Frei M., Oyen A., Anders M. D., Bateson L., Guerrieri L., Comerci V., Steen A. H. (2020). The Evolution of Wide-Area DInSAR: From Regional and National Services to the European Ground Motion Service. *Remote Sensing*, 12(12):2043-2043.

Crozier M.J. (2010). Deciphering the effect of climate change on landslide activity: a review. *Geomorphology*, 124 (3–4), 260–267.

Drahor M. G., Gökturkler G., Berge M. A. (2006). Application of electrical resistivity tomography technique for investigation of landslides: a case from Turkey. *Environmental Geology*, 49(7): 147-155.

Fattahi, H., & Amelung, F. (2013). DEM error correction in InSAR time series. *IEEE Transactions on Geoscience and Remote Sensing*, 51(7), 4249-4259.

Funning, G.J., Parsons, B., Wright, T.J., Jackson, J.A. and Fielding, E.J. (2005). Surface displacements and source parameters of the 2003 Bam (Iran) earthquake from Envisat advanced synthetic aperture radar imagery. *Journal of Geophysical Research: Solid Earth*, 110(B9).

Guo C. B., Yan Y. Q., Zhang Y. S., Zhang X. J., Zheng Y. Z., Li X., Yang Z. H., Wu R. (2021). Study on the Creep-Sliding Mechanism of the Giant Xiongba Ancient Landslide Based on the SBAS-InSAR Method, Tibetan Plateau, China. *Remote Sensing,*13(17): 3365-3365.

Han L. B., Zhou C., He N., He J. S., Wu Y. (2014) Analytical Solution on Progressive Deformation and Initiation of Landslide from the Sliding Interface. *Chinese Journal of Underground Space and Engineering*, 10(06): 1342-1347 (in Chinese).

Hu J. (2008). Research on using InSAR to detect three-dimensional ground deformation [Doctoral dissertation, Central South University].

Hu, X., Lu, Z., Pierson, T.C., Kramer, R., George, D.L. (2018). Combining InSAR and GPS to determine transient movement and thickness of a seasonally active low-gradient translational landslide. *Geophysical Research Letter*, 45 (3), 1453–1462.

Huang X., Garcia M. H. (1998). A Herschel-Bulkley model for mud flow down a slope. *Journal of Fluid Mechanics*, 374:305-333.

Jin J. J. (2021) Study on the development characteristics and stability of the Xiongba giant ancient landslide in the Jinshajiang Fault Zone. *Chinese Academy of Geological Sciences*.

Ji Y. J., Lv L. X. (2021). M-Decomposed Least Squares and Recursive Least Squares Identification Algorithms for Large-Scale Systems. *Ieee Access*, 9:139466-139472.

Jonsson S.,(2002). Fault Slip Distribution of the 1999 Mw 7.1 Hector Mine, California, Earthquake, Estimated from Satellite Radar and GPS Measurements [J]. *Bulletin of the Seismological Society of America*, 92(4): 1377-1389.

Lv J. C., Zhang R., Bao X., Wu R. Z., Hong R. K., He X., Liu G. X. (2025). Time-series InSAR landslide three-dimensional deformation prediction method considering meteorological time-delay effects. *Engineering Geology*, 350.

Li X., Guo C. B., Yang Z. H., Liao W., Wu R., Jin J. J., He Y. X. (2021). Development Characteristics and Formation Mechanism of the Xiongba Giant Ancient Landslide in the Jinshajiang Tectonic Zone. *Geoscience,*, 35(01): 47-55.

Li Y G, Wang. L., Zhao Y., Wang H. P., Li S. S., Jia J. F. (2022). Numerical investigation of the flow characteristics of Bingham fluid on a slope with corrected smooth particle hydrodynamics. *Frontiers in Environmental Science*, 10.

Lin, Q., Steger, S., Pittore, M., Zhang, J., Wang, L., Jiang, T., Wang, Y. (2022). Evaluation of potential changes in landslide susceptibility

https://doi.org/10.5194/egusphere-2026-2324
Preprint. Discussion started: 15 June 2026

and landslide occurrence frequency in China under climate change. *Science of the total environment*, 850, 158049.

Liu G., Guo H. D., Perski Z.,Fan J. H.,Bai S. B.,Yan S. Y.,Song R. (2016). Monitoring the slope movement of the Shuping landslide in the Three Gorges Reservoir of China, using X-band time series SAR interferometry[J]. Advances in Space Research, 57(12): 2487-2495.

Liu M., Yang W. T., Yang Y. T., Guo L. L., Shi P. J. (2023).Identify Landslide Precursors from Time Series InSAR Results. *International Journal of Disaster Risk Science*, 14(6):963-978.

Muller J. R., Martel S. J., (2000). Numerical models of translational landslide rupture surface growth [J]. *Pure and Applied Geophys*, 157(6–8): 1009–1038.

Min D. B., Choi S. H., Lu J. B., Ham B., Sohn K., Do M. N. (2014). Fast Global Image Smoothing Based on Weighted Least Squares. *IEEE Transactions on Image Processing*, 23(12):5638-5653.

Nikolaeva, E., Walter, T.R., Shirzaei, M., Zschau, J. (2014). Landslide observation and volume estimation in central Georgia based on L-band InSAR. *Natural Hazards Earth System Sciences*, 14 (3), 675–688.

Okada Y.,(1985). Surface deformation due to shear and tensile faults in a half-space [J]. *Bulletin of the Seismological Society of America*, 75(4): 1135-1154.

Pepe, A., Euillades, L. D., Manunta, M., & Lanari, R. (2011). New advances of the extended minimum cost flow phase unwrapping algorithm for SBAS-DInSAR analysis at full spatial resolution. *IEEE Transactions on Geoscience and Remote Sensing*, 49(10), 4062-4079.

Sabharwal A., Potter L. C. (1998). Convexly constrained linear inverse problems: Iterative least-squares and regularization. *IEEE Transactions on Image Processing,* 46(9):2345-2352.

Sadeghi Z., Wright T. J., Hooper A. J., Novellino A., Bateson L., Biggs J., Jordan C. (2021). Benchmarking and inter-comparison of Sentinel-1 InSAR velocities and time series. *Remote Sensing of Environment*, 256:112306.

Simeoni L., Mongiovì L. (2007). Inclinometer Monitoring of the Castelrotto Landslide in Italy. *Journal of Geotechnical and Geoenvironmental Engineering*, 133(6): 653-666.

Song C., Yu C., Li Z., Utili S., Frattini P., Crosta G., Peng J. (2022). Triggering and recovery of earthquake accelerated landslides in Central Italy revealed by satellite radar observations. *Nature Communications*, 13 (1), 7278.

Stark T. D., Choi H. (2008). Slope inclinometers for landslides. *Landslides*, 5(3): 339-350.

Su M. B. (1987). Quantification of Cable Deformation with Time Domain Reflectometry Techniques. Evanston: Northwestern University.

Wu D. H., Hao L. N., Yan L. H., Tang F. S., Zheng G. (2024). InSAR－based detection and deformation factor analysis of landslide clusters in the Jinsha River, J. *Remote Sensing for Natural Resources*, 36(3): 259－266.

Xu C. J, Wang L. Y., Wen Y. M., Wang J. J. (2011). Strain Rates in the Sichuan-Yunnan Region Based upon the Total Least Squares Heterogeneous Strain Model from GPS Data. *Terrestrial Atmospheric and Oceanic Sciences*, 22(2):133-147.

Yan Y. Q., Guo C. B., Zhang Y. S., Zhang X. J., Zheng Y. Z., Li X., Yang Z. H., Wu R. J. (2021). Study of the deformation characteristics of the Xiongba ancient landslide based on SBAS-InSAR method, Tibet, China. *Acta Geologica Sinica*, 95(11): 3556-3570.

Yan Y., Guo C., Zhang Y., Qiu Z. D., Li C. G., Li X. (2024). Development and Deformation Characteristics of Large Ancient Landslides in the Intensely Hazardous Xiongba-Sela Section of the Jinsha River, Eastern Tibetan Plateau, China. *J. Earth Sci*,. 35(3):980–997.

Yan Y., Yu H. W., Yang T. L. (2025). A Multitemporal Baseline Phase Unwrapping Approach for Accurately Monitoring High-Gradient Deformation With Two-Pass DInSAR. *Ieee Transactions On Geoscience And Remote Sensing*, 63.

Yang, Y. H., Tsai, M. C., Hu, J. C., Aurelio, M. A., Hashimoto, M., Escudero, J. A. P., ... & Chen, Q. (2018). Coseismic slip deficit of the 2017 Mw 6.5 Ormoc earthquake that occurred along a creeping segment and geothermal field of the Philippine fault. *Geophysical Research Letters*, 45(6), 2659-2668.

Yang Y. H., Xu Q., Xie L., Xu Q., Hu J. C., Chen Q. (2024). Landslide Thickness Estimated from InSAR-Derived 2D Deformation: Application to the Xiongba Ancient Landslide, China. *Remote Sensing*, 16(24):4689.

Yu H. H., Cai G. L., Gan Q., Shen D. (2020). Early Identification of the Jiangdingya Landslide of Zhouqu Based on SBAS-InSAR Technology. *Earthquake Research in China*, 34(4):510-522.

https://doi.org/10.5194/egusphere-2026-2324
Preprint. Discussion started: 15 June 2026

Yunjun, Z., Fattahi, H., & Amelung, F. (2019). Small baseline InSAR time series analysis: Unwrapping error correction and noise reduction. *Computers & Geosciences*, 133, 104331.

Zheng S. X., Wang J., Yan Y., Liu W., Zhao H., Yang J. X., Fan X. A., Zhang Y., Wang M., Yu T. B. (2024). Development characteristics and river blocking outburst analysis of Shadong landslide in the upper reaches of Jinsha River. *Hydrogeology & Engineering Geology*, 51(6):160-170.

Zhang H. X. (2010). Extracting coseismic deformation field related to the 5.12 wenchuan earthquake by alos dinsar and numerical modeling. Doctoral dissertation, Southwest Jiaotong University.

Zhu, W., Yang, L., Cheng, Y., Liu, X. and Zhang, R. (2024). Active thickness estimation and failure simulation of translational landslide using multi-orbit InSAR observations: A case study of the Xiongba landslide. *International Journal of Applied Earth Observation and Geoinformation*, 129: 103801.